Liao *et al. Biology Direct* (2025) 20:40
https://doi.org/10.1186/s13062-025-00639-6

Biology Direct

RESEARCH Open Access

Dynamic single-cell transcriptomic reveals the cellular heterogeneity and a novel fibroblast subpopulation in laryngotracheal stenosis

Ziwei Liao[1], Yangyang Zheng[1], Mingjun Zhang[1], Xiaoyan Li[1*], Jing Wang[1*] and Hongming Xu[1*]

Abstract

Background Laryngotracheal stenosis (LTS), a pathological narrowing of the upper airway caused by excessive extracellular matrix (ECM) deposition, often leads to dyspnea and even respiratory failure. However, systematic studies addressing the specific subpopulations and their contribution to LTS development still remain underexplored.

Results We collected laryngotracheal tissue at multiple time points of LTS rat model, established by injuring their laryngotracheal lining, and performed dynamic single-cell RNA sequencing (scRNA-seq) to elucidate the transcriptomic atlas of LTS development. The results showed, from the inflammatory state to the repair/fibrotic state, infiltration of immune cells such as monocyte macrophages decreased and fibroblast increased. We delineated the markers and functional status of different fibroblasts subsets and identified that fibrotic fibroblasts may originate from multiple fibroblast subpopulations, including a new subpopulation characterized by the expression of chondrogenic markers such as Ucma and Col2a1, we designated this subcluster as chondrocyte injury-related fibroblasts (CIRF). Furthermore, we categorized monocytes/macrophages into several subtypes and identified that SPP1 high macrophages represented the largest macrophage subpopulation in LTS, providing evidence to clarify the importance of SPP1 macrophages in fibrosis disease. Our findings also revealed the interactions among these cells to explore the molecular mechanism associated with LTS pathogenesis.

Conclusions Our study, for the first time, conducted dynamic scRNA-seq on LTS, revealing the cellular heterogeneity and providing a valuable resource for exploring the intricate molecular landscape of LTS. We propose CIRF may represent a tissue-specific fibroblast lineage in LTS and potentially originate from cells in the perichondrium of the trachea and transform into fibrotic fibroblasts. Integration of our study with those of other respiratory fibrotic diseases will allow for a comprehensive understanding of airway remodeling in respiratory diseases and exploring potential new therapeutic targets for their treatment.

Keywords Single-cell RNA sequencing, Laryngotracheal stenosis, Airway stenosis, Fibroblasts, Fibrosis, Macrophages

*Correspondence:
Xiaoyan Li
chhshent@126.com
Jing Wang
wangjing80s@163.com
Hongming Xu
xuhongming@188.com
[1]Department of Otorhinolaryngology Head and Neck Surgery, Shanghai Children's Hospital, Shanghai Jiao Tong University School of Medicine, No. 355, Luding Road, Shanghai 200062, People's Republic of China

Background

Laryngotracheal stenosis (LTS) is a pathological narrowing of the upper airway caused by excessive extracellular matrix (ECM) deposition [1]. Symptoms of LTS include dysphonia, dyspnea, stridor, and even respiratory failure, depending on the site and degree of stenosis [2]. LTS can arise from various etiologies, including congenital disease, trauma, chemical injury, specific and non-specific inflammation, and some unknown cause, of which long-term endotracheal intubation is the most common [3]. With the frequent occurrence of public health events, such as the COVID-19, tracheal intubation, on the one hand, serves as an important tool for treating critical care patients with lung failure [4], but also leads to an increased risk of LTS [5, 6]. Surgical operation is the only way to treat the LTS nowadays [7, 8], but limited by high recurrence of re-stenosis and severe complications [9]. Limitations of treatment methods make prevention of the formation of LTS very crucial.

Excessive ECM deposition is the primary pathophysiological factor for initiation and maintenance of LST [10], therefore, fibroblasts, which drive matrix deposition and stiffening [11], have been the focus of LTS research [12, 13]. Even though advanced experimental techniques have revealed significant diversity and functional heterogeneity within fibroblast populations in LTS [14, 15], there still lack of a systematic study addressing the tissue-specific fibroblast lineages in LTS, as well as their contribution to LTS development.

Additionally, macrophages are another predominant cell population in LTS [16], and have traditionally been classified into M1 and alternatively activated M2 phenotypes [17]. Recent studies, however, have demonstrated that macrophages consist of various subpopulations with distinct functions, surpassing the conventional M1/M2 classification [18–20]. Despite this, the abnormalities and significance of these macrophage subpopulations in LTS remain largely unexplored. Therefore, the mechanisms underlying the interactions and effects of fibroblasts, macrophages, and immune cells in LTS require further investigation.

Single-cell RNA sequencing (scRNA-seq) has emerged as a powerful tool for deciphering complex cell-to-cell communication and identifying novel biological markers in various diseases [21–23]. Dynamic gene expression at the single-cell level can reflect development, differentiation, or disease progression [24]. Increasing evidence suggests that scRNA-seq is invaluable for exploring the temporal heterogeneity of altered cell types in fibrotic diseases, including cardiac and renal fibrosis [25, 26]. However, to date, the cellular composition and functional alterations in LTS, particularly among fibroblast and macrophage subsets, as well as the underlying mechanisms, remain poorly understood.

For the first time, we performed dynamic single-cell transcriptomic profiling of LTS rat model collected from different time during LTS development, aiming to uncover cell subpopulations distinct from those in other fibrotic tissues and provided new insights on LTS evolution and development. Our finding provided a valuable resource for exploring the intricate molecular landscape of LTS, which allows for in-depth understanding on LTS and offers potential new therapeutic targets for its treatment.

Methods

Establishment of injury-induced rat model of LTS

All animal experiments were conducted in accordance with the guidelines of the Institutional Animal Care and Use Committee of Shanghai Children's Hospital. LTS was induced in 12-week-old male rats. Anesthesia was administered via an intraperitoneal injection of ketamine (100 mg/kg) and xylazine (10 mg/kg). After sterilizing the skin with ethanol, a 1.5 cm vertical midline ventral incision was made over the laryngotracheal complex to expose the larynx and trachea. A 0.22 μm wire brush was inserted into the airway and scraped back and forth to create a circumferential laryngotracheal injury, thereby inducing LTS. Following surgery, the rats were maintained on a high-protein soft diet (ClearH_2O) [27]. Some rats were sacrificed at 1 and 7 days post-surgery, and their laryngotracheal complexes were harvested for histological analysis ($n = 6$ for each time point). Additionally, some rats were sacrificed at 1, 3, 5, and 7 days post-surgery, and their laryngotracheal lining tissues were collected, dissected into 1 mm^3 pieces, and prepared for scRNA-seq analysis ($n = 3$ for each time point).

Histology and immunohistochemical staining of LTS tissue

Laryngotracheal tissues were harvested from rats at 1 and 7 days post-injury. After fixation in 4% PFA for 24 h and embedding in paraffin, the tissues were sectioned into 4 μm-thick slices in the axial plane. The sections were then subjected to Hematoxylin and Eosin (H&E) staining and Masson staining. For immunohistochemical staining, the tissue sections were blocked with 3% BSA and incubated overnight at 4 °C with primary antibodies, including rabbit anti-rat α-SMA (ab5694; Abcam) and rabbit anti-rat COL1A1 (72026T; CST). On the following day, goat anti-rabbit secondary antibodies were applied. All stained sections were digitized using a slide scanner, and quantitative analysis was performed using ImageJ. Thickness measurements were conducted from the medial aspect of the tracheal cartilage to the basement membrane of the epithelium, with the thickest portion of each segment measured and recorded.

Sample collection and single-cell suspension Preparation

Rats were sacrificed at 1, 3, 5, and 7 days post-injury, and their laryngotracheal lining tissues were collected for sequencing ($n = 3$ for each time point). After being washed twice in PBS, each sample was dissected into 1 mm^3 pieces and digested in sCelLiveTM tissue dissociation solution for 30 min at 37 °C. Following digestion, the cells were filtered through a 40 μm cell strainer and centrifuged at 800 × g for 5 min. The supernatant was then removed, and the pellet was washed once with PBS at 400 × g for 5 min. The pellet was resuspended in PBS supplemented with 1% FBS. Cell viability was assessed using the Trypan blue exclusion method, and the resulting single-cell suspension had a viability rate of over 80%.

10 × genomics library and sequencing

Single-cell sequencing was performed using the 10× Genomics platform by LC-Bio Technology Co., Ltd. (Hangzhou, China). Following the manufacturer's standard protocol, library sequencing was conducted on the Illumina NovaSeq sequencing system (paired-end multiplexing run, 150 bp). The cell suspension was loaded into a 10× Chromium chip to capture single cells and generate single-cell gel beads in emulsions (GEMs). The process included reverse transcription (RT) reactions, GEM-RT clean-up, cDNA amplification, cDNA fragmentation, end-repairing, A-tailing, and ligation to an index adaptor, followed by single-cell libraries construction.

Quality control and cell clustering

For quality control, Seurat (version 4.3.0) was used to assess unique molecular identifiers (UMIs) and mitochondrial gene content. Cells with more than 500 detected genes and less than 25% mitochondrial gene content were considered to have passed quality control. A total of 47,068 cells met the quality control criteria and were retained for subsequent bioinformatic analysis. Library size normalization was performed on the filtered matrix to obtain normalized counts, and the top 2,000 variable genes were identified with the parameter flavor = 'Seurat'. Principal component analysis (PCA) was conducted on the scaled variable gene matrix to reduce dimensionality, with the top 50 principal components used for clustering and further dimensional reduction. In this study, cells were grouped into 30 clusters using a graph-based clustering approach and visualized with Uniform Manifold Approximation and Projection (UMAP) or t-Distributed Stochastic Neighbor Embedding (t-SNE).

Pseudotime trajectory analysis

The trajectory analysis of cell differentiation was constructed with Monocle2 (v 2.10.0) to reveal the cell-state transitions. The "DDRTree" function was applied to reduce the dimensions with default settings and map the differentiation of fibroblast subtypes. The results were visualized by "plot_cell_trajectory" function.

Enrichment analysis

Gene Ontology (GO) and Kyoto Encyclopedia of Genes and Genomes (KEGG) enrichment analysis were used to predict the molecular function, biological function, cellular composition, biological process and possible pathways involved in differentially expressed genes. KEGG and GO analyses were performed by cluster Profiler R package and visualized by ggplot2 R package. P-values < 0.05 were considered significantly enriched.

Calculation of macrophage polarization scores

"AddModuleScore" function in Seurat were used to calculate the polarization score of cells annotated as "Monocytes" and "Macrophages", and evaluate the functional polarization of Monocytes and Macrophages.

Cell–cell communication analysis

The Cellphone DB (version 4.0.0) software equipped with a detailed receptor–ligand database was used to identify potential interactions between different cells [28]. Permutation number for calculating the null distribution of average ligand-receptor pair expression in randomized cell identities was set to 1000. The threshold for individual ligand or receptor expression was based on the cut-off value of average log gene expression in each cell type. Predicted interaction pairs with p-value < 0.05 and an average log2 expression fold change > 0.1 were considered significant. The results were visualized by "heatmap_plot" and "dot_plot".

Statistical analysis

All data analyses were performed by using R software, ImageJ and GraphPad Prism. When comparing differences between two groups, statistical analysis was performed and analyzed by Student's t-test, when comparing differences among three or more groups were performed and analyzed by one-way analysis of variance (ANOVA). P values < 0.05 were considered statistically significant.

Results

Establishment of a rat model of LTS

We induced laryngotracheal stenosis (LTS) in 12-week-old male rats and collected samples at multiple time points during disease progression (1, 3, 5, and 7 days post-laryngotracheal injury; $n = 3$ for each time point) (Fig. 1a). To validate the successful induction of the rat LTS model prior to performing scRNA-seq, we first stained laryngotracheal tissue from rats at 1- and 7-days post-injury ($n = 3$ per group) (Fig. 1b). Hematoxylin and eosin (H&E) staining of the laryngotracheal tissue

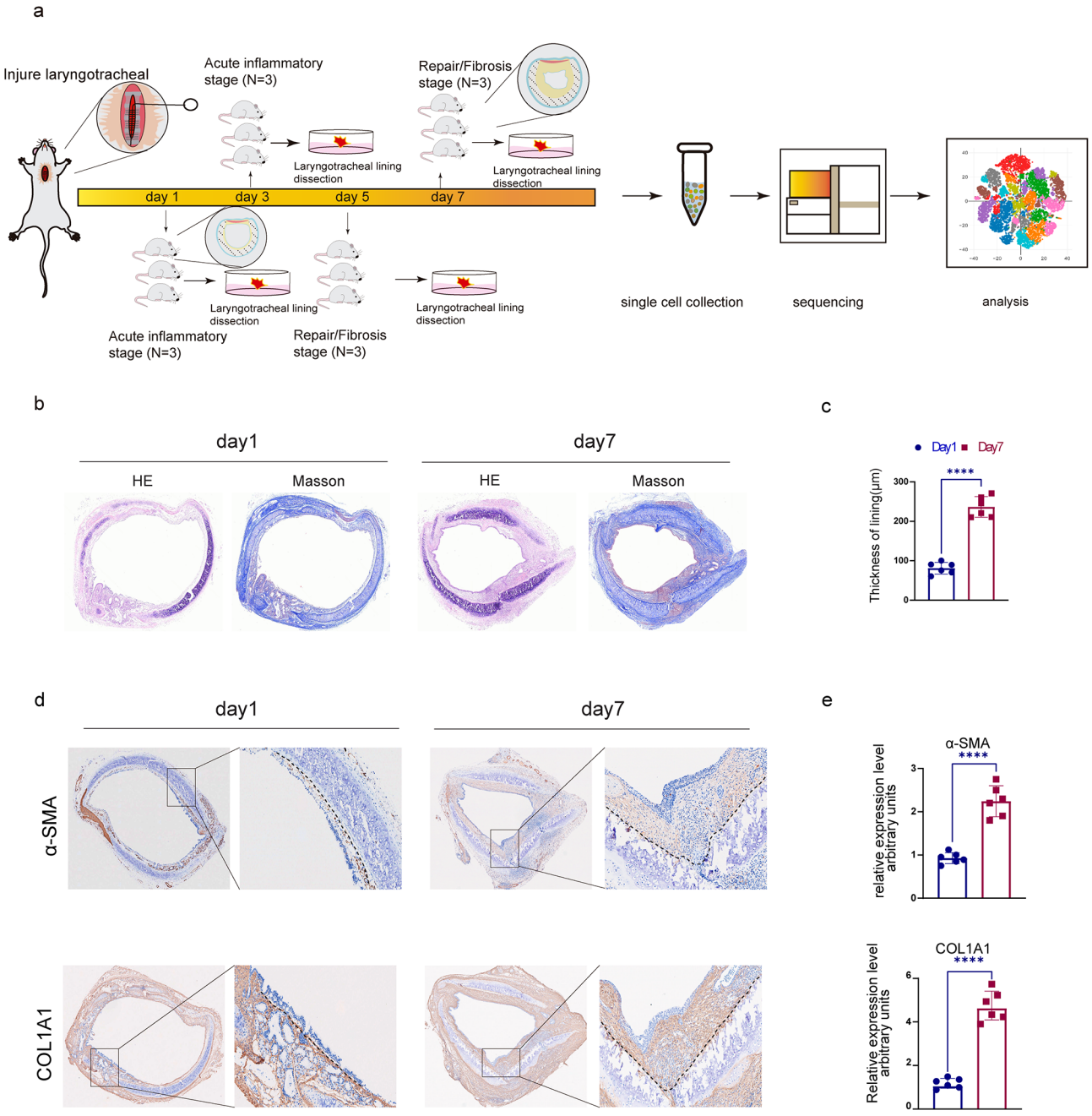

Fig. 1 Schematic representation of the experimental procedure and validation of rat model of LTS. (**a**) Workflow: The rat model of LTS was induced by injuring the laryngotracheal lining using a brush. Laryngotracheal complexes were harvested at 1 and 7 days post-injury for histological analysis ($n=6$). Laryngotracheal lining tissues were collected at 1, 3, 5, and 7 days post-injury, dissected, and processed for single-cell RNA sequencing (scRNA-seq) ($n=3$ for each time point). (**b**) Representative images of Hematoxylin and Eosin (H&E) staining and Masson's trichrome staining. (**c**) Quantification of the laryngotracheal lining thickness was shown. Data are presented as mean ± SEM, with statistical significance determined by Student's t-test. *$P<0.05$; ****$P<0.0001$ between indicated groups. (**d**) Representative images of immunostaining for Col1a1 and α-SMA of laryngotracheal tissues from rats at 1 and 7 days post-LTS induction. $N=6$. (**e**) Quantification of the expression levels of Col1a1 and α-SMA was shown on the right side. Data are presented as mean ± SEM, with statistical significance determined by Student's t-test. *$P<0.05$; ****$P<0.0001$ between indicated groups

revealed that the laryngotracheal lining in 7-days post-injury rats was significantly thicker than in 1-day, with the thickened lining causing severe airway obstruction. Masson's trichrome staining further confirmed successful LTS induction, as collagen deposition was significantly increased in 7-days post-injury rats ($n=3$) compared to 1-day rats ($n=3$) (Fig. 1c). Additionally, immunohistochemical analysis demonstrated enhanced expression of Collagen 1A1 and α-SMA in 7-days post-injury rats relative to 1-day rats, indicating increased extracellular

matrix deposition in the tissues (Fig. 1d and e). Therefore, we successfully established a rat model of LTS for subsequent studies.

Single-cell landscape of the pathologic progression of LTS

To characterize the heterogeneity of cells during injury and repair stage, and to associate bulk transcriptomic changes with specific cell types, we performed scRNA-seq on the laryngotracheal lining of rats. Following stringent quality control filtering and removal of doublets, a total of 47,068 cells (Day 1 = 12,720; Day 3 = 9,909; Day 5 = 11,642; Day 7 = 12,797) passed quality metrics and were included for downstream normalization, principal component analysis (PCA), and Harmony integration (Fig. 2a). Visualization of single-nucleus transcriptomes in Uniform Manifold Approximation and Projection (UMAP) space identified 30 distinct cell clusters (Fig. 2b and c). The top 10 most highly expressed genes in each cluster were shown in Fig. 2c and d.

Using established cell type-specific marker genes, we identified 8 distinct cell types within these 30 clusters: Fibroblasts (expressing Col1a1, Col1a2, Mgp, Bgn), Pericytes (expressing Rgs5, Abcc9, Kcnj8), Endothelial cells (expressing Vwf, Pecam1, Cdh5), Epithelial cells (expressing Wfdc2, Gpx2, Sfn), Neutrophils (expressing S100a9 and S100a8), Monocytes/Macrophages (expressing Cd14, Fcgr3a, Van, Cd163, Mrc1), T cells (expressing Cd3g and Cd3e), and a small cluster lacking distinct marker genes. The scaled expression levels and proportions of cells expressing cluster-specific markers for each cell type were shown in dot plots (Fig. 2e).

By comparing UMAP visualizations and cell ratios, we observed dynamic changes in the proportions of cell clusters at each time point. Following LTS induction, there was a notable increase in the proportion of fibroblasts. Fibroblast constituted the largest cluster, proving their critical role in LTS, while the proportions of epithelial and myeloid cells gradually decreased. Additionally, the proportions of endothelial cells and pericytes exhibited fluctuating changes over time (Fig. 2f and g). In conclusion, using scRNA-seq, we identified various cell populations and their gene markers during the progression of LTS. Further analysis will focus on the subpopulations within these cell groups and their characteristics.

Gene signatures of different fibroblasts subsets in LTS

To further elucidate the specific role of fibroblasts in LTS, we performed unsupervised clustering on all fibroblast populations. Common fibroblast lineage-specific markers, including Col1a1, Col1a2, Col3a1, and Mgp (Fig. 3a), were used to validate the fibroblast clusters identified by SingleR. Based on gene expression patterns (Fig. 3b), we identified 8 distinct subpopulations: fibrotic, inflammatory, stress-activated, proliferating, chondrocyte injure related fibroblasts (CIRF), epithelial-mesenchymal transition (EMT) related fibroblasts (EMTF), mesothelial, and "other." The top differentially expressed genes for each subpopulation were listed in Fig. 3c. UMAP space showed these distinct subpopulations of fibroblasts (Fig. 3d).

Inflammatory fibroblasts exhibited high expression of Cxcl12 and were characterized by the specific expression of multiple complement factors, such as C7, C4a, and C4b, which were associated with the early recruitment of inflammatory cells [29]. Stress-activated fibroblasts expressed interferon-responsive genes, including Ifitm1 and Ifitm2 [30, 31]. Proliferating fibroblasts were marked by the expression of the proliferation marker protein Ki-67 [32], along with other proliferation-associated genes such as Cenpt, Ube2c, and Stmn2 (Fig. 3c). Fibrotic fibroblasts, which were significantly increased in LTS, were characterized by the high expression of extracellular matrix (ECM) component protein genes, including Postn, Col1a1, and Col5a1, as well as ECM regulatory genes such as Tnfaip6 and Lcn (Fig. 3e). Most importantly, we identified a unique subpopulation characterized by the expression of Ucma and other chondrogenic markers, including Col2a1, Col9a2, and Col10a1. We named this subpopulations CIRF (chondrocyte injury related fibroblasts) (Fig. 3f). EMTF fibroblasts exhibited high expression of epithelial markers such as Krt16 and Krt13, suggesting that these cells may be undergoing EMT, a process implicated in the pathogenesis of fibrosis (Fig. 3G). In contrast, the "other" cluster lacked distinct marker genes and did not exhibit notable differential expression compared to other subpopulations. In summary, we identified a novel fibroblast subpopulation in LTS that highly expresses chondrogenic markers.

Functional characterization of fibroblast subpopulations

To further explore the roles of these fibroblast clusters, we performed Gene Ontology (GO) and Kyoto Encyclopedia of Genes and Genomes (KEGG) enrichment analyses. The CIRF cluster was enriched for terms such as "chondrocyte differentiation", "glycosaminoglycan binding", "skeletal system development", "bone development", and "positive regulation of mesenchymal stem cell differentiation." Notably, pathways associated with extracellular matrix (ECM) production and organization were also enriched in CIRF, suggesting that CIRF may function as ECM-producing cells. Pathways involved in chondrocyte remodeling, and ECM regulation were significantly upregulated in CIRF, including "PI3K-Akt signaling pathway," "Focal Adhesion", "ECM-receptor interaction", and "TNF signaling pathway" (Fig. 4a). Additionally, KEGG analysis revealed that the upregulated genes in the EMTF subpopulations were associated with epithelial-mesenchymal transition (EMT), including pathways such

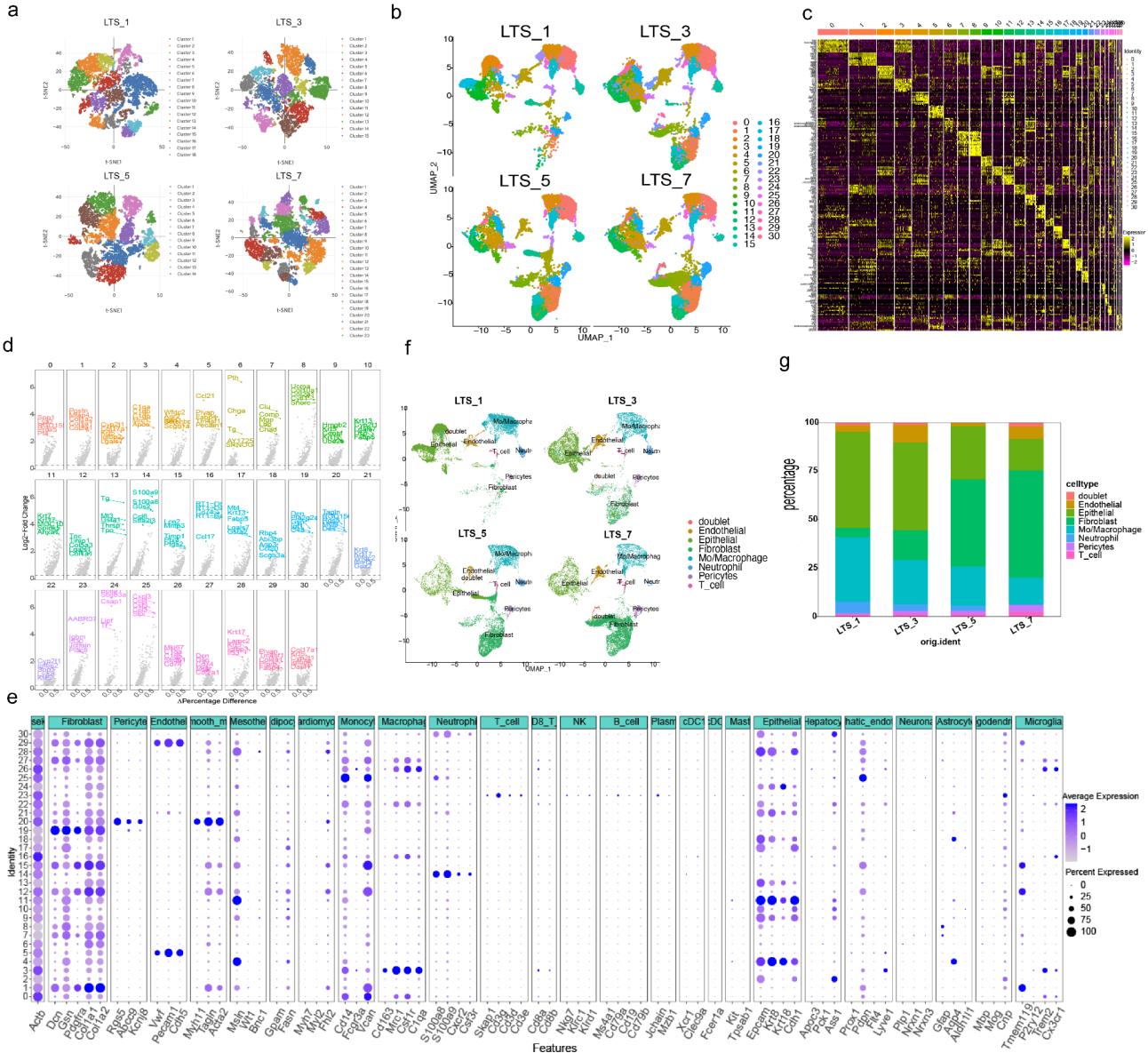

Fig. 2 The cellular compositions of the pathologic progression of LTS. (**a**) t-SNE plots the distribution of cells at different time points (LTS_1, LTS_3, LTS_5, and LST_7) based on clustering results. Each cell was represented as a dot, with cells colored according to their assigned clusters. (**b**) Manifold Approximation and Projection (UMAP) plots shown the distribution of 30 cell clusters at LTS_1, LTS_3, LTS_5, and LTS_7, with distinct cell clusters annotated in different colors. (**c**) Principal component heatmap displayed the expression level of the top 10 differentially expressed genes (DEGs) across the 30 cell clusters, with each column representing a cell. Color reflected the expression level, from low (purple) to intermediate (black)and high (yellow). (**d**) Volcano plots highlighted the top 5 differentially expressed genes (DEGs) in each cell cluster. The Y-axis represents the log2 fold change, indicating the magnitude of gene expression change, while the X-axis reflects the percentage of cells expressing the DEGs. (**e**) Dot plot illustrated the signature gene expression in each cell cluster. Dot color intensity denoted average expression level, from low to high. Dot size was proportional to the fraction of cells expressing each gene. (**f**) UMAP plots demonstrated major 8 cell types existing in LTS_1, LTS_3, LTS_5, and LTS_7, including doublet, endothelial cell, endocardial cell, fibroblast, mo/macrophage, neutrophil, pericyte, T cell, along with their distribution across these time points. Distinct cell types were annotated by different colors. Bar chart exhibited the composition of cell populations at different time points. Blocks represented distinct time LTS_1, LTS_3, LTS_5, and LTS_7. The quantity of cell was in proportion to the block height

as TGF-β, HIF-1, Rap1, and cAMP signaling pathways (Fig. 4b). In the fibrotic fibroblast cluster, upregulated genes were primarily involved in ECM-related processes, including "collagen-containing extracellular matrix", "collagen fibril organization", and "extracellular matrix structural constituent". ECM-related pathways such as "ECM-receptor interaction", "PI3K-Akt signaling pathway", and "Relaxin signaling pathway" were also enriched in the fibrotic subpopulation (Fig. 4c).

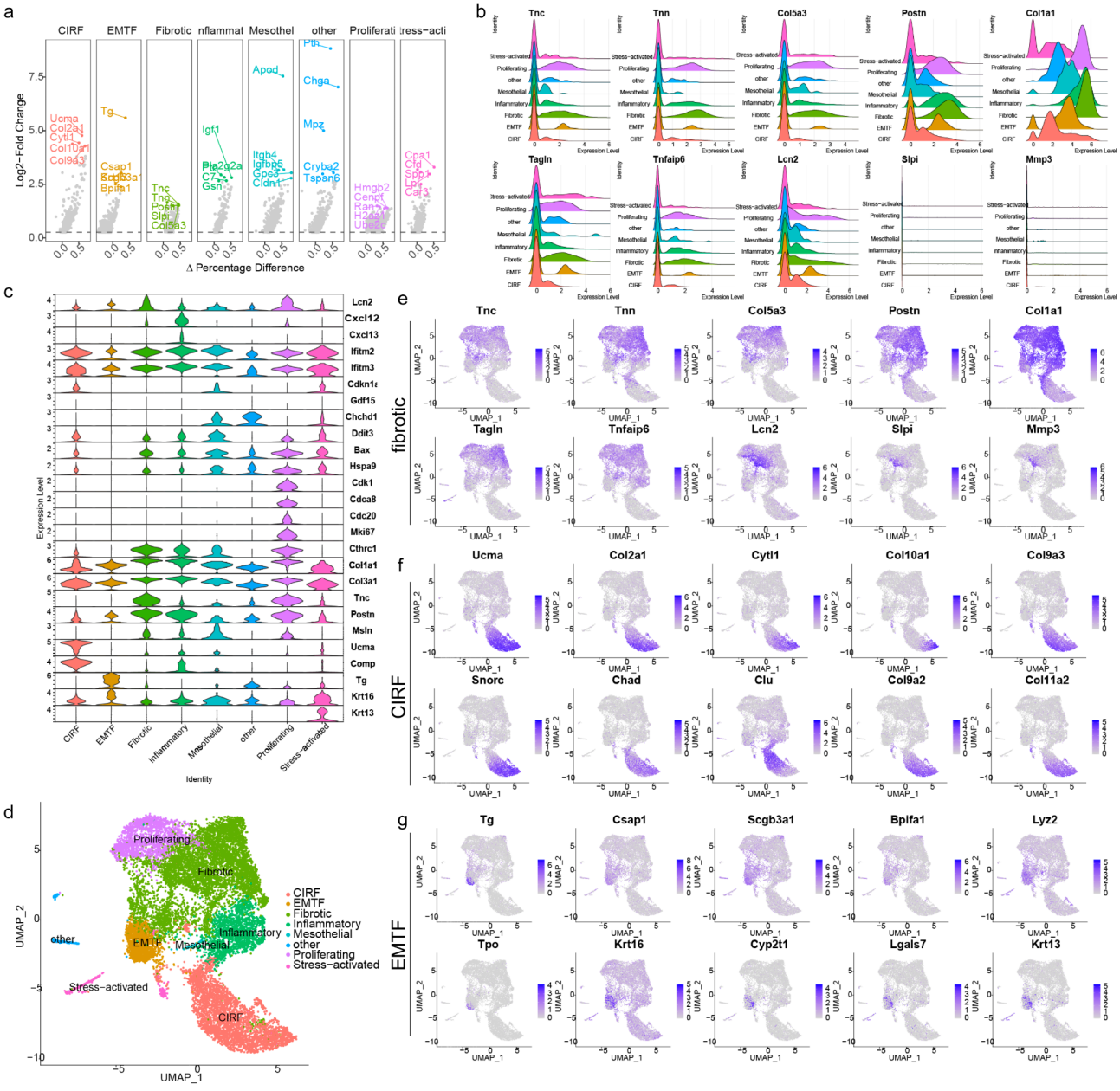

Fig. 3 Gene signatures of different fibroblasts subset in LTS. (**a**) Volcano plot highlighted the top 5 differentially expressed genes (DEGs) in each cell type. The Y-axis represented the log2 fold change, indicating the magnitude of gene expression change, while the X-axis showed the percentage of cells expressing each DEG. (**b**) Ridge plots illustrated the expression profiles of 10 common Fibroblast lineage-specific markers across each cell type. The curves represented kernel density estimates (KDE), with the height of the curve corresponding to the density of gene expression within each region. (**c**) Violin plot showed the expression levels of selected marker genes in each fibroblast subpopulation. The width of the plot indicated the distribution of gene expression, reflecting the density of cells at different expression levels. (**d**) UMAP plot depicted 8 distinct fibroblast subpopulations identified during LTS progression, including fibrotic, inflammatory, stress-activated, proliferating, chondrocyte injury-related fibroblasts (CIRF), epithelial-mesenchymal transition (EMT)-related fibroblasts (EMTF), mesothelial, and "other." Each subpopulation was annotated with a unique color. (**e**) Feature plots illustrated the expression of specific genes in fibrotic fibroblasts, alongside the spatial distribution of gene expression across the fibroblast population. The color intensity reflected the level of expression, ranging from low to high. (**f**) Feature plots illustrated the expression of specific genes in CIRF, alongside the spatial distribution of gene expression across the fibroblast population. The color intensity reflected the level of expression, ranging from low to high. (**g**) Feature plots illustrated the expression of specific genes in EMTF, alongside the spatial distribution of gene expression across the fibroblast population. The color intensity reflected the level of expression, ranging from low to high

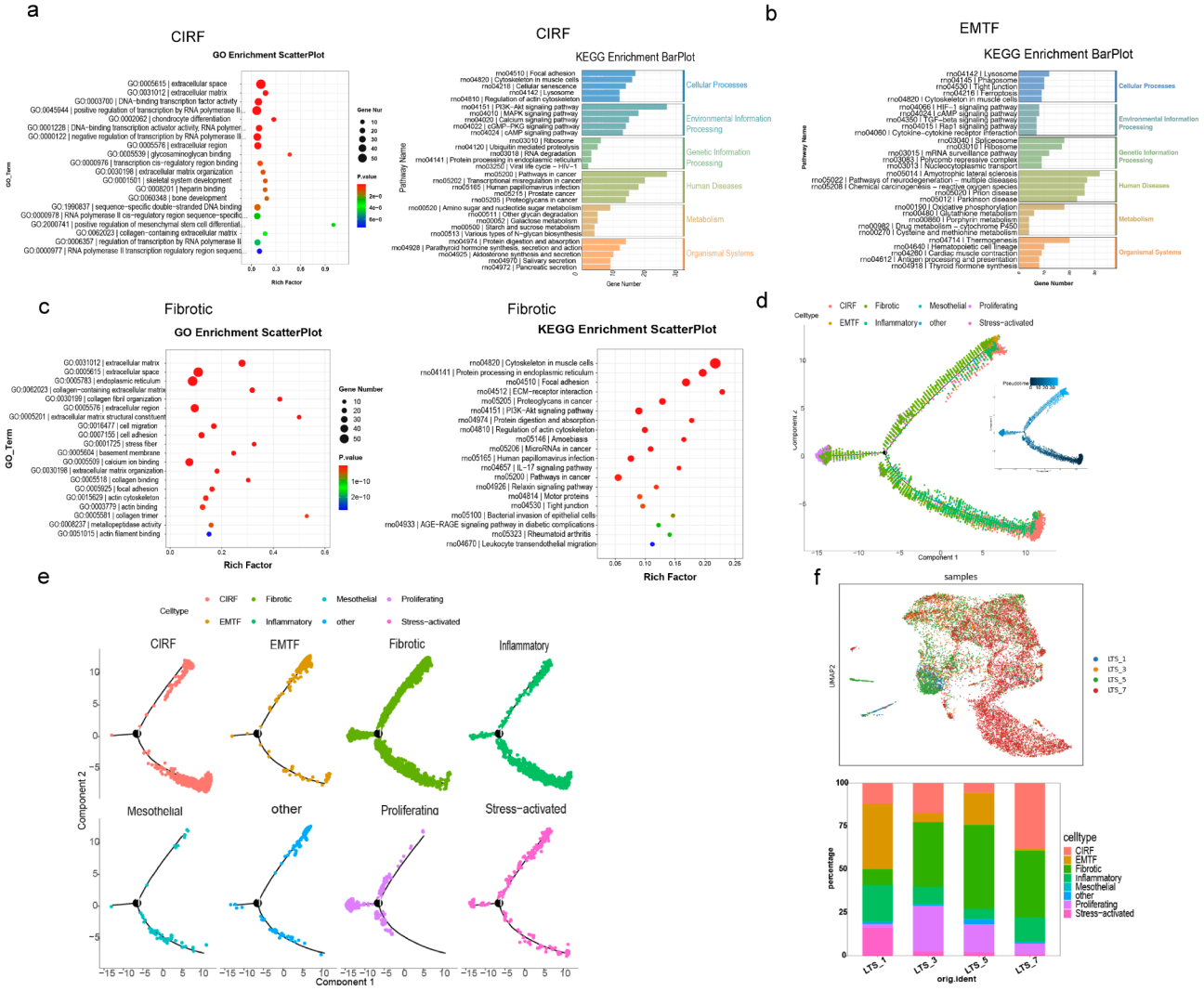

Fig. 4 Functional characterization of different fibroblast. (**a**)GO enrichment scatterplot displayed the top 20 significantly enriched biological processes based on upregulated genes identified in CIRF. Dot color represented the p-value, from high(green) to low (red), and dot size was proportional to the number of associated genes. The X-axis showed the enrichment factor. KEGG enrichment bar plot illustrated the enriched pathways based on upregulated genes in CIRF with the bar length corresponding to the number of related genes. (**b**) KEGG enrichment bar plot displayed the enriched pathways based on upregulated genes identified in EMTF. The length of each bar was proportional to the number of related genes. (**c**) The GO enrichment scatterplot visualized the top 20 significantly enriched biological processes based on upregulated genes identified in fibrotic fibroblasts, while the KEGG enrichment scatterplot presented the top 20 most significantly enriched pathways. In both plots, dot color reflected the p-value, ranging from high (green) to low (red), and dot size was proportional to the gene number associated with each process or pathway. Value on X-axis represented the Rich Factor. (**d**) The pseudo-time trajectory provided an overview of the distribution of fibroblast subpopulations along the pseudo-time trajectory, with each subpopulation represented by a distinct color. And the pseudo-time trajectory, depicted as a blue line, with color intensity representing pseudo-time progression from dark blue (early stages) to light blue (later stages) as a temporal reference. (**e**) Trajectory analysis separately illustrated the detailed distribution of the eight fibroblast subpopulations along the pseudo-time trajectory. (**F**) UMAP maps displayed the distribution of fibroblast at different time points: LTS_1 (1 day after LTS induction), LTS_3 (3 days), LTS_5 (5 days), and LTS_7 (7 days), with cells from the same time point represented by the same color. Bar chart showed the fraction of fibroblast subpopulations at each time point, with each block representing distinct time points (LTS_1, LTS_3, LTS_5, and LTS_7). The quantity of cell was proportional to the block height

To investigate the origin of CIRF and the relationships among fibroblast subpopulations, we performed pseudo-time trajectory analysis (Fig. 4d). The analysis revealed that CIRF and inflammatory fibroblasts were primarily located at the origin of the differentiation trajectory, whereas EMTF, proliferating, and stress-activated fibroblasts were concentrated at the ends of different trajectory branches. Interestingly, EMTF and stress-activated fibroblasts shared a common differentiation endpoint. Fibrotic fibroblasts were evenly distributed along the trajectory, spanning from the origin to the ends of the branches. These results suggest that fibrotic fibroblasts may arise from multiple fibroblast subpopulations, including CIRF, while only a small fraction of CIRF may

transition from other fibroblast subpopulations (Fig. 4e). By combining these results with the functional phenotype of CIRF, we inferred that CIRF may originate from cells in the perichondrium [33].

To further evaluate the pathological progression of LTS, we compared the proportions of each fibroblast subpopulation at different time points. Compared to Day 1 (LTS_1), the proportion of fibrotic fibroblasts significantly increased, becoming the largest cluster at Days 3 (LTS_3) and 5 (LTS_5). Notably, the predominant subpopulation transitioned from fibrotic fibroblasts to CIRF by Day 7 (LTS_7), driven by a significant increase in CIRF proportions. Additionally, the frequencies of inflammatory, stress-activated, and EMTF fibroblasts peaked and be the predominant subpopulation at LTS_1, but decreased at later time points, while the proportion of proliferating fibroblasts increased at LTS_3 before declining at later stages as well (Fig. 4f). Taken together, the novel CIRF subpopulation we identified may originate from cells in the perichondrium and eventually transform into fibrotic fibroblasts, along with other fibroblast subpopulations such as EMTF.

Single cell profiles of monocytes/macrophages in LTS

Macrophages play a critical role in fibrosis. To further elucidate the specific functions of macrophages in LTS, we conducted unsupervised clustering of all myeloid cells. We used common specific markers of the myeloid cell lineage, including Lyz2, Cd74, Rt1-da, Rt1-db1, Spp1, Ctss, and Lgmn, to validate the myeloid cell clusters defined by SingleR (Fig. 5a). Visualization of single-cell transcriptomes in UMAP space revealed 16 distinct cell clusters (Fig. 5b). The top 10 genes with the highest expression in each separate cell cluster were shown in Fig. 5c. Based on gene expression patterns, we further identified 9 subpopulations, including cDC1, cDC3, macro_C1qc, macro_IL1b, macro_mki67, macro_spp1, monocyte, neutrophil, and others (Fig. 5d and g).

To evaluate the pathological progression of LTS, we compared the proportions of each macrophage subpopulation across different time points. The macro_spp1 cluster was the largest, with its proportions fluctuating significantly, showing an increase at LTS_5 but a decrease at LTS_7. Notably, although macro_mki67 constituted a small proportion, it continued to increase. The frequencies of macro_IL1b and neutrophils peaked at LTS_3 before decreasing at later time points. Besides, there was little change in the proportion of macro_C1qc (Fig. 5e).

Macrophages can polarize into classically activated M1 phenotypes, which have pro-inflammatory functions, or alternatively activated M2 phenotypes, which exhibit anti-inflammatory and pro-fibrotic functions. We calculated the M1 and M2 polarization scores for myeloid cell clusters. The gene expression signatures of the 16 clusters did not conform to canonical M1 or M2 classifications, indicating a reprogrammed phenotype with mixed M1 and M2 features. The M2 scores of macrophage clusters 1, 2, 3, 4, 5, 6, 7, 8, 11, 12, 13, and 15 were higher than the M1 scores, indicating a predominant role for M2 polarization in LTS progression. However, macrophage clusters 9, 10, and 14 (corresponding to cDC1, macro_IL1b, and monocyte) exhibited higher M1 scores, suggesting a distinct polarization pattern in these clusters. (Fig. 5f). In summary, we identified several macrophage subpopulations, among which the macro_spp1 subpopulation has previously been found to be associated with fibrosis. Notably, these subpopulations did not exhibit significant M1/M2 polarization.

Cell-cell communication reveals the interaction patterns between fibroblast and macrophage subpopulations

To investigate cell–cell interactions during LTS progression, we employed computational modeling using CellPhoneDB to identify interactions between fibroblasts and macrophages (Fig. 6a). The interactions within fibroblast populations were notably stronger than those with macrophages (Fig. 6a). The intercellular crosstalk between fibrotic fibroblast (highly expressing Postn) and other fibroblast populations was most frequency. Studies revealed that the supernatant of Postn + fibroblasts could increase the expression of collagens in other fibroblasts [34], suggesting that fibroblast cell-cell communication played a crucial role in LTS. In particular, the interactions between macro_Mki67 and fibroblasts, as well as those between fibroblasts and monocytes, were significantly enhanced. Conversely, EMTF exhibited the weakest interactions with other cell populations. The interactions between CIRF and various fibroblast and macrophage subpopulations were also found (Fig. 6b). Among the ligand–receptor pairs involving macrophage subpopulations and CIRF, APP-CD74 was significantly enriched in dendritic cells (cDC1 and cDC3). What's more, APP-CD74 was also enriched in ETMF/cDC1. Fibrotic fibroblast expressed the highest diversity of ligand types that bind to CIRF receptors. Other notable ligand–receptor pairs involving interactions between CIRF and different fibroblast and macrophage subpopulations included Fibronectin 1 (FN1)-Integrin aVb1 and FN1-Integrin a5b1 (Fig. 6b).

To characterize the fibroblast- macrophage communication specific to LTS, we utilized the CellPhoneDB tool to explore potential ligand-receptor interactions from our high-resolution scRNA-seq data. Fibrotic, CIRF, mesothelial, and macrophage subpopulations emerged as the predominant communication 'hub' in LTS, despite the number and strength of cell interactions being significantly different. Notably, CIRF-fibroblast interactions

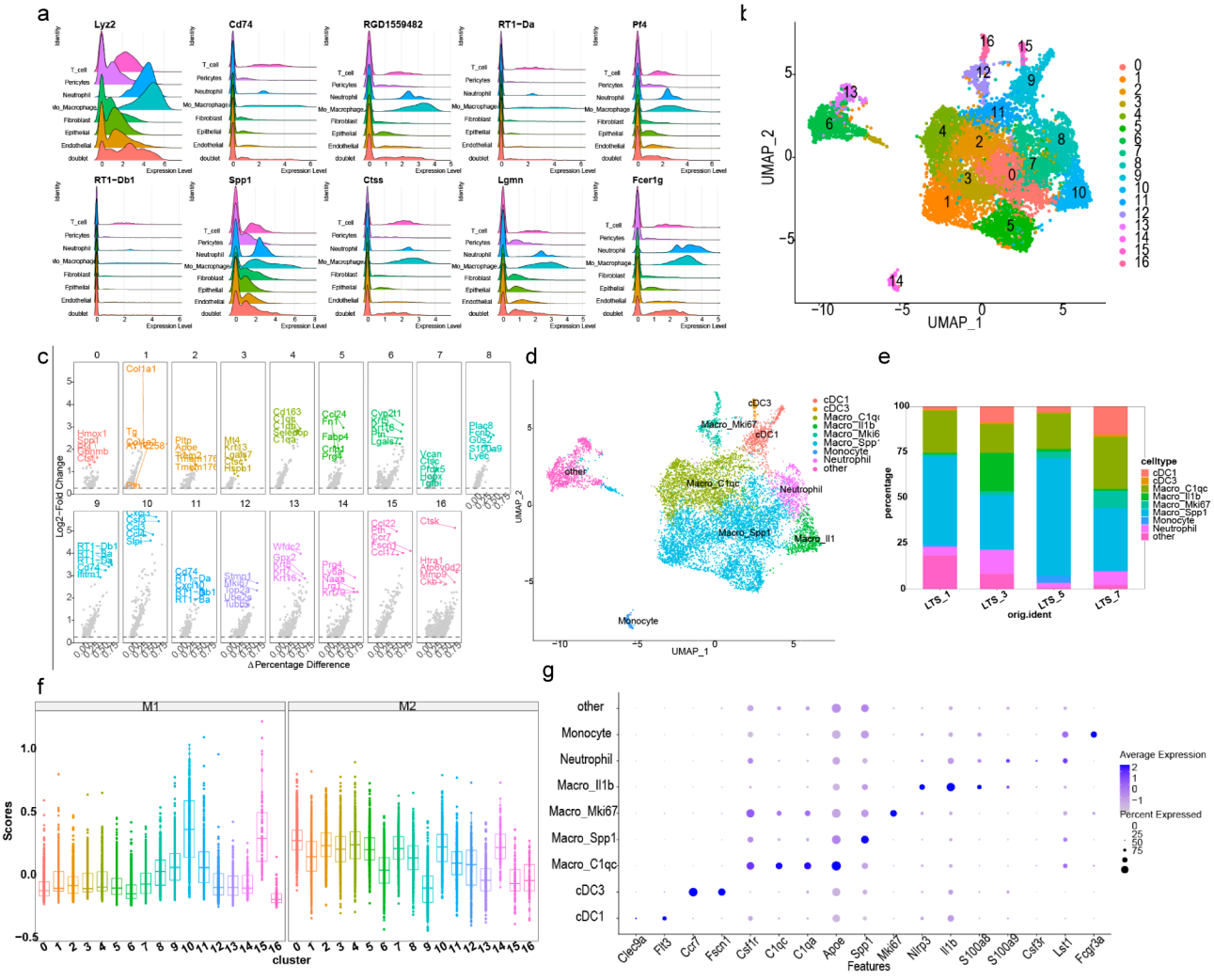

Fig. 5 Single-cell landscape of macrophage subpopulations in LTS. (**a**) Ridge plots displayed the expression signatures of 10 common myeloid lineage-specific markers for each cell type. The curves represented the KDE, with the height indicating the density in the region. (**b**) UMAP plots showed 16 distinct myeloid cell clusters identified during LTS progression, with each cluster annotated by a different color. (**c**) Volcano plot highlighted the top 5 DEGs in each myeloid cell cluster. The Y-axis represented the log2-fold change, indicating the magnitude of gene expression change, while the X-axis reflected the percentage of cells expressing each DEG. (**d**) UMAP plots demonstrated 9 distinct myeloid cell subpopulations found during LTS procession. Each subpopulation was annotated by a different color. (**e**) Bar chart shown the fraction of myeloid cell subpopulations at each time point. Blocks represented distinct time points: LTS_1(1 day after LTS induction), LTS_3 (3 days), LTS_5 (5 days), and LTS_7 (7 days). The block height was proportional to the number of cells at each time point. (**f**) Biological functional scores showed the M1/M2 polarization scores for each cell cluster. The middle horizontal line represented the median, with the upper and lower edges of the box indicating the third and first quartiles, respectively. (**g**) Dot plot illustrated the gene expression signatures of myeloid cell subpopulation. Dot color intensity represented the average expression level, ranging from low to high and dot size was proportional to the fraction of cells expressing the gene

and fibrotic-fibroblast interactions were the most obvious. (Fig. 6c and d).

Discussion

Fibroblasts are recognized as the main contributors to LTS [12, 35]. In this study, we identified eight fibroblast subpopulations in our rat LTS samples using scRNA-seq, including fibrotic, inflammatory, stress-activated, proliferating, CIRF, EMTF, mesothelial, and other subtypes (Fig. 3b). By analyzing single-cell data, we found that fibrotic fibroblasts (characterized by high expression of Postn) significantly increased and be the largest subpopulation in the middle stage of LTS progression. GO and KEGG enrichment analyses indicated that upregulated genes in the fibrotic fibroblast cluster were primarily associated with ECM-related processes and pathways, suggesting that fibrotic fibroblasts contribute to collagen formation in LTS [24]. Our findings were consistent with previous studies that Postn + fibroblasts could influence the LTS development through TGF-β/RHOA Pathway [36]. Actually, the expression of Postn in fibroblasts had also been implicated in other fibrotic diseases, such

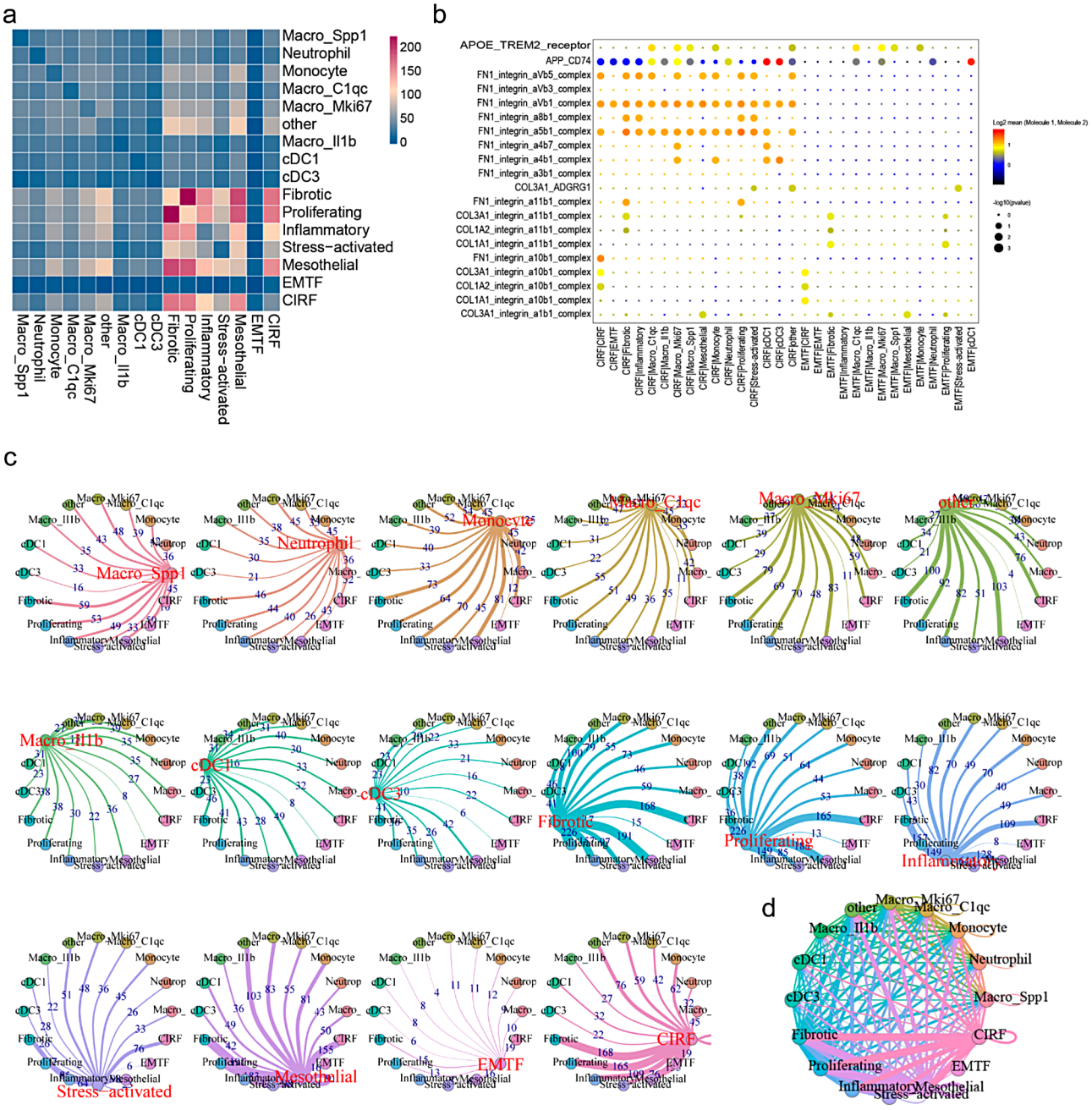

Fig. 6 The interactions between fibroblast and macrophage subpopulations. (**a**) Heatmap showed the intercellular crosstalk between macrophage and fibroblast subpopulations during LTS procession. The Color represented the frequency of cell–cell communication, ranging from low (blue) to high (red). (**b**) Dot plots displayed the ligand-receptor interaction pairs between CIRF/EMTF fibroblast and macrophage subpopulations. Dot color indicated the communication probability, from low (black) to high (red), while dot size was inversely proportional to the p-value. (**c**) Network plots illustrated the interaction number between fibroblast and macrophage subpopulations. Each dot represented a single cell subpopulation. The width of the lines connecting cell clusters was proportional to the number of interactions, and the color of the lines corresponded to the source cell cluster. The numbers on the connecting lines quantified the significant ligand-receptor pairs between any two cell clusters. Loops indicated autocrine signaling circuits. (**d**) Network plot showed the overall interaction networks between fibroblast and macrophage subpopulations, summarizing the broader intercellular communication

as idiopathic pulmonary fibrosis and keloids [37, 38]. Notably, we identified a unique fibroblast subpopulation characterized by the high expression of Ucma and other chondrogenic maker [39]. As this subpopulation had not been previously reported, we named it CIRF (chondrocyte injury-related fibroblasts). GO and KEGG enrichment analyses of CIRF revealed that this cluster was also enriched in ECM-related processes and pathways, indicating that CIRF contribute to collagen formation as well. Interestingly, CIRF was significantly enriched

in gene ontology terms such as chondrocyte differentiation and glycosaminoglycan binding, as well as pathways associated with chondrocyte remodeling. An increase in CIRF during LTS was observed. Pseudotime trajectory analysis showed that CIRF was primarily located at the origin of the differentiation trajectory. Combining these findings with the functional phenotype of CIRF, we hypothesize that CIRF may originate from cells in the perichondrium of tracheal cartilage [33]. We also identified a subpopulation with high expression of epithelial markers, suggesting these cells may be undergoing EMT, which we named EMTF. Previous studies have suggested that bile acids may contribute to LTS by inducing EMT [40], and other investigations have shown that inhibiting EMT could alleviate the progression of LTS [41, 42], highlighting the critical role of EMT in LTS development. Pseudotime trajectory analysis revealed that inflammatory fibroblasts were primarily located at the origin of the differentiation trajectory, while stress-activated fibroblasts were positioned at the end, shedding light on the relationship between inflammatory and stress-activated fibroblasts. Due to the limited understanding of these fibroblast subpopulations, further studies and additional direct experimental evidence are needed to elucidate the origins and functions of this unique fibroblast subpopulation in LTS.

Macrophages play crucial roles in regulating LTS progression. Using scRNA-seq, we categorized monocytes/macrophages into five subtypes: macro_C1qc, macro_IL1b, macro_mki67, macro_spp1, and monocytes, based on their dominant gene expression profiles. Macro_spp1, which highly expresses SPP1 (commonly referred to as SPP1 + macrophages), had been identified in several recent studies as fibrosis-associated macrophages [43, 44]. A study demonstrated that Spp1 + macrophages expanded in both human chronic kidney disease and heart failure, promoting cardiac and renal fibrosis by orchestrating fibroblast activation through Spp1, Fn1, and Sema3 crosstalk [45]. Moreover, previous studies indicated that Spp1 + macrophages interact with cancer-associated fibroblasts (CAFs) to stimulate ECM remodeling and promote tumor immune barrier structure formation [46]. These findings suggested that the interaction between Spp1 + macrophages and fibroblasts played a crucial role in collagen formation. Additionally, Spp1 marked a conserved macrophage injury response that masks fibrosis-specific programming in the lung, further implicating its potential role in fibrosis [47]. In our study, Spp1 + macrophages constituted the largest macrophage subpopulation, suggesting that they might play a significant role in LTS. Macro_IL1b exhibited higher expression levels of the pro-inflammatory factor IL1b [48], and its M1 scores were higher than those of M2. Our results further supported previous research showing that serum IL-1β levels in LTS patients were higher than those in healthy controls, suggesting a positive correlation between IL-1β and LTS [49]. A previous study revealed that pro-inflammatory M1 macrophages could induce a pro-fibrotic response in adipose-derived stem cells (ASCs) through IL1b expression [50], aligning with other findings that blocking macrophage IL1b signaling could suppress fibroblast activation and ameliorate cardiac fibrosis [51]. These findings suggested that macro_IL1b might play a dual role in LTS progression, contributing to both pro-inflammatory and pro-fibrotic functions. Further molecular biology studies are required to elucidate the role of macro_IL1b in LTS fibrosis.

Advanced research indicated that fibroblast-macrophage crosstalk plays a critical role in fibrosis progression across multiple organs [52]. In our study, we observed that fibroblast subpopulations interacted with all macrophage subpopulations identified. Interestingly, interactions within fibroblast populations were notably stronger than those between fibroblasts and macrophages. Among these, intercellular crosstalk between fibrotic fibroblasts (characterized by high Postn expression) and other fibroblast populations was the most frequent. Functional studies havd shown that the supernatant of Postn + fibroblasts could increase collagen expression in other fibroblasts [34], suggesting that interactions within fibroblast populations could serve as a potential therapeutic target for fibrotic diseases. Furthermore, fibrotic fibroblasts were found to highly express ECM regulatory genes such as Tnfaip6 and Lcn [53, 54]. Due to article length constraints, we focused on the interactions between CIRF/EMTF and macrophage. Notably, we found that APP-CD74 receptor interactions were significantly enriched in CIRF-cDC1 as well as EMTF-cDC1, indicating the central role of the APP-CD74 pathway in LTS development. Previous studies havd shown that the APP-CD74 axis mediated endothelial cell-macrophage communication, promoting kidney injury and fibrosis [55]. Furthermore, a cell communication analysis revealed that the APP-CD74 axis was significantly upregulated in biliary atresia, contributing to the positive regulation of fibroblast proliferation and liver fibrosis [56]. These findings suggested that the APP-CD74 axis played a particularly important role in promoting fibrotic diseases. However, the role of the APP-CD74 axis in regulating LTS development remains unexplored, and further investigation are required. Notably, fibrotic fibroblasts expressed the highest diversity of ligand types binding to CIRF receptors, further highlighting their importance in regulating other fibroblasts. Additional studies are needed to determine whether Postn + fibroblast is a unique marker of fibrotic fibroblasts capable of regulating other fibroblast populations and to elucidate how this type of fibroblast uniquely contributes to the development of LTS.

Additionally, in this study, we aimed to point out the cellular heterogeneity at different time points during the laryngotracheal stenosis (LTS) process. Given the ethical and practical challenges of obtaining human samples at different stages, we used a rat LTS model and performed single-cell RNA sequencing. Therefore, while this model provided valuable insights into the dynamics of cellular changes during LTS, including the communication between fibroblasts and macrophages, the findings might not fully reflect the complexity of human LTS. Moreover, we did not conduct further experimental validation to assess the functional relevance of the observed gene expression patterns and cell subpopulations. Future research involving human samples and additional experimental validation will be crucial to confirm these findings and better understand the biological roles of the identified subpopulations in LTS.

Conclusion

In conclusion, we conducted a systematic analysis of fibroblast and macrophage subpopulations and their interactions in LTS using scRNA-seq. We identified a unique fibroblast subpopulation characterized by high Ucma expression, which may originate from cells in the perichondrium of tracheal cartilage. Additionally, we explored the potential role of fibrotic fibroblasts in producing ECM component proteins and regulating other fibroblast populations. Furthermore, we investigated the interactions between fibroblasts and macrophages during LTS progression and identified specific ligand-receptor pairs mediating fibroblast-macrophage communication in LTS. These findings provide deeper insights into the development of LTS and may help identify potential therapeutic targets for its treatment.

Abbreviations

LTS	Laryngotracheal stenosis
ECM	Excessive extracellular matrix
ScRNA-seq	Single-cell RNA sequencing
EMT	Epithelial-mesenchymal transition
EMTF	EMT related fibroblasts
CIRF	Chondrocyte injury related fibroblasts
GO	Gene Ontology
KEGG	Kyoto Encyclopedia of Genes and Genomes
UMAP	Manifold Approximation and Projection
T-SNE	T-Distributed Stochastic Neighbor Embedding

Acknowledgements

Not applicable.

Author contributions

ZWL and JW analyzed data; YYZ and MJZ performed project administration and interpreted the data; ZWL and JW was a major contributor in writing the manuscript; XYL and HMX reviewed and edited the manuscript; HMX and JW acquired the funding. All authors read and approved the final manuscript.

Funding

This study was supported by National Natural Science Foundation of China (No. 82171121 and No. 82272270) and the Science and Technology Commission of Shanghai Municipality Funds (22ZR1451700).

Data availability

The datasets generated and analysed during the current study are available in the n the NCBI Sequence ReadArchive (SRA) database with the accession number PRJNA1221101. https://dataview.ncbi.nlm.nih.gov/object/PRJNA1221101?reviewer=1s3v0bituc3m2h9opgguav31g.

Declarations

Ethics approval and consent to participate

All animal experiments were conducted in accordance with the guidelines of the Institutional Animal Care and Use Committee of Shanghai Children's Hospital (2021RY024-E01). In this study, 12-week-old male rats were used.

Consent for publication

Not applicable.

Competing interests

The authors declare no competing interests.

Received: 12 February 2025 / Accepted: 20 March 2025
Published online: 31 March 2025

References

1. Xu M, Hu B, Chen J, Wang J, Li X. Mechanisms of fibrosis in iatrogenic laryngotracheal stenosis: new discoveries and novel targets. Biomed Pharmacother. 2024;170:115995.
2. Motz KM, Lina IA, Samad I, Murphy MK, Duvvuri M, Davis RJ et al. Sirolimus-eluting airway stent reduces profibrotic Th17 cells and inhibits laryngotracheal stenosis. JCI Insight. 2023;8(11).
3. Freitas C, Martins N, Novais-Bastos H, Morais A, Fernandes G, Magalhães A. The role of interventional bronchoscopy in the management of post-intubation tracheal stenosis: A 20-year experience. Pulmonology. 2021;27(4):296–304.
4. Sparling JL, Chitilian HV, Korn E, Alfille PH, Bao X. Induction of anaesthesia and airway management in patients with severe tracheal stenosis: a single-centre retrospective study. Br J Anaesth. 2025;134(1):250–2.
5. Chen Y, Wen W, Du X, Wang H, Zhu L, Wang S et al. Retrospective analysis of factors contributing to poor prognosis among 271 pediatric patients with tracheal stenosis treated with slide tracheoplasty. J Thorac Cardiovasc Surg. 2024. https://doi.org/10.1016/j.jtcvs.2024.11.017
6. Duggan LV, Mastoras G, Bryson GL. Tracheal intubation in patients with COVID-19. CMAJ. 2020;192(22):E607.
7. Wei S, Zhang Y, Luo F, Duan K, Li M, Lv G. Tissue-engineered tracheal implants: advancements, challenges, and clinical considerations. Bioeng Transl Med. 2024;9(4):e10671.
8. Tapias LF, Lanuti M, Wright CD, Hron TA, Ly A, Mathisen DJ, et al. COVID-19-related Post-intubation tracheal stenosis: early experience with surgical treatment. Ann Surg. 2022;275(1):e271–3.
9. Yang M, Li H, Zhou Y, Li H, Wei H, Cheng Q. Airway collapse hinders recovery in bronchoscopy therapy for postintubation tracheal stenosis patients. Eur Arch Otorhinolaryngol. 2024;281(6):3061–9.
10. Karagiannidis C, Velehorschi V, Obertrifter B, Macha HN, Linder A, Freitag L. High-level expression of matrix-associated transforming growth factor-beta1 in benign airway stenosis. Chest. 2006;129(5):1298–304.
11. Hoeft K, Koch L, Ziegler S, Zhang L, Luetke S, Tanzer MC et al. ADAMTS12 promotes fibrosis by restructuring extracellular matrix to enable activation of injury-responsive fibroblasts. J Clin Invest. 2024;134(18).
12. Motz K, Samad I, Yin LX, Murphy MK, Duvvuri M, Ding D, et al. Interferon-γ treatment of human laryngotracheal Stenosis-Derived fibroblasts. JAMA Otolaryngol Head Neck Surg. 2017;143(11):1134–40.
13. Zhang G, Xue C, Zeng Y. β-elemene alleviates airway stenosis via the ILK/Akt pathway modulated by MIR143HG sponging miR-1275. Cell Mol Biol Lett. 2021;26(1):28.
14. Lina IA, Berges A, Ospino R, Davis RJ, Motz KM, Tsai HW, et al. Identifying phenotypically distinct fibroblast subsets in type 2 Diabetes-Associated iatrogenic laryngotracheal stenosis. Otolaryngol Head Neck Surg. 2022;166(4):712–9.

15. Talatala ERR, Clark E, Ye W, Davis RJ, Hillel AT, Collins SL, et al. Localizing hormone receptor expression to cellular compartments in idiopathic subglottic stenosis. Laryngoscope. 2023;133(12):3506–11.
16. Hillel AT, Samad I, Ma G, Ding D, Sadtler K, Powell JD, et al. Dysregulated macrophages are present in Bleomycin-Induced murine laryngotracheal stenosis. Otolaryngol Head Neck Surg. 2015;153(2):244–50.
17. Motz K, Lina I, Murphy MK, Drake V, Davis R, Tsai HW, et al. M2 macrophages promote collagen expression and synthesis in laryngotracheal stenosis fibroblasts. Laryngoscope. 2021;131(2):E346–53.
18. Ospino R, Berges A, Mafla L, Collins S, Li YC, Lina I, et al. Characterizing the macrophage population in patients with idiopathic subglottic stenosis. Laryngoscope. 2023;133(9):2308–16.
19. MacParland SA, Liu JC, Ma XZ, Innes BT, Bartczak AM, Gage BK, et al. Single cell RNA sequencing of human liver reveals distinct intrahepatic macrophage populations. Nat Commun. 2018;9(1):4383.
20. Wu MM, Yang YC, Cai YX, Jiang S, Xiao H, Miao C, et al. Anti-CTLA-4 m2a antibody exacerbates cardiac injury in experimental autoimmune myocarditis mice by promoting Ccl5-Neutrophil infiltration. Adv Sci (Weinh). 2024;11(34):e2400486.
21. Papalexi E, Satija R. Single-cell RNA sequencing to explore immune cell heterogeneity. Nat Rev Immunol. 2018;18(1):35–45.
22. Gazzinelli-Guimaraes PH, Dulek B, Swanson P, Lack J, Roederer M, Nutman TB. Single-cell molecular signature of pathogenic T helper subsets in type 2-associated disorders in humans. JCI Insight. 2024;9(7).
23. Sheng B, Pan S, Ye M, Liu H, Zhang J, Zhao B, et al. Single-cell RNA sequencing of cervical exfoliated cells reveals potential biomarkers and cellular pathogenesis in cervical carcinogenesis. Cell Death Dis. 2024;15(2):130.
24. Tsukui T, Wolters PJ, Sheppard D. Alveolar fibroblast lineage orchestrates lung inflammation and fibrosis. Nature. 2024;631(8021):627–34.
25. Ruiz-Villalba A, Romero JP, Hernández SC, Vilas-Zornoza A, Fortelny N, Castro-Labrador L, et al. Single-Cell RNA sequencing analysis reveals a crucial role for CTHRC1 (Collagen triple helix repeat containing 1) cardiac fibroblasts after myocardial infarction. Circulation. 2020;142(19):1831–47.
26. Conway BR, O'Sullivan ED, Cairns C, O'Sullivan J, Simpson DJ, Salzano A, et al. Kidney Single-Cell atlas reveals myeloid heterogeneity in progression and regression of kidney disease. J Am Soc Nephrol. 2020;31(12):2833–54.
27. Hillel AT, Namba D, Ding D, Pandian V, Elisseeff JH, Horton MR. An in situ, in vivo murine model for the study of laryngotracheal stenosis. JAMA Otolaryngol Head Neck Surg. 2014;140(10):961–6.
28. Efremova M, Vento-Tormo M, Teichmann SA, Vento-Tormo R. CellPhoneDB: inferring cell-cell communication from combined expression of multi-subunit ligand-receptor complexes. Nat Protoc. 2020;15(4):1484–506.
29. Cavagnero KJ, Li F, Dokoshi T, Nakatsuji T, O'Neill AM, Aguilera C et al. CXCL12 + dermal fibroblasts promote neutrophil recruitment and host defense by recognition of IL-17. J Exp Med. 2024;221(4).
30. Unali G, Crivicich G, Pagani I, Abou-Alezz M, Folchini F, Valeri E, et al. Interferon-inducible phospholipids govern IFITM3-dependent endosomal antiviral immunity. Embo J. 2023;42(10):e112234.
31. Buchrieser J, Degrelle SA, Couderc T, Nevers Q, Disson O, Manet C, et al. IFITM proteins inhibit placental syncytiotrophoblast formation and promote fetal demise. Science. 2019;365(6449):176–80.
32. Stamatiou K, Huguet F, Serapinas LV, Spanos C, Rappsilber J, Vagnarelli P. Ki-67 is necessary during DNA replication for fork protection and genome stability. Genome Biol. 2024;25(1):105.
33. Matsushita Y, Chu AKY, Tsutsumi-Arai C, Orikasa S, Nagata M, Wong SY, et al. The fate of early perichondrial cells in developing bones. Nat Commun. 2022;13(1):7319.
34. Deng CC, Hu YF, Zhu DH, Cheng Q, Gu JJ, Feng QL, et al. Single-cell RNA-seq reveals fibroblast heterogeneity and increased mesenchymal fibroblasts in human fibrotic skin diseases. Nat Commun. 2021;12(1):3709.
35. Xu M, Hu B, Chen J, Zhao L, Wang J, Li X. CXCR7 promotes the migration of fibroblasts derived from patients with acquired laryngotracheal stenosis by NF-κB signaling. Transl Pediatr. 2023;12(9):1634–45.
36. She Z, Chen H, Lin X, Li C, Su J. POSTN regulates fibroblast proliferation and migration in laryngotracheal stenosis through the TGF-β/RHOA pathway. Laryngoscope. 2024;134(9):4078–87.
37. Wu S, Liu M, Zhang M, Ye X, Gu H, Jiang C, et al. The gene expression of CALD1, CDH2, and POSTN in fibroblast are related to idiopathic pulmonary fibrosis. Front Immunol. 2024;15:1275064.
38. Hong YK, Hwang DY, Yang CC, Cheng SM, Chen PC, Aala WJ, et al. Profibrotic subsets of SPP1(+) macrophages and POSTN(+) fibroblasts contribute to fibrotic scarring in acne keloidalis. J Invest Dermatol. 2024;144(7):1491–e50410.
39. Surmann-Schmitt C, Dietz U, Kireva T, Adam N, Park J, Tagariello A, et al. Ucma, a novel secreted cartilage-specific protein with implications in osteogenesis. J Biol Chem. 2008;283(11):7082–93.
40. Aldhahrani A, Powell J, Ladak S, Ali M, Ali S, Verdon B, et al. The potential role of bile acids in acquired laryngotracheal stenosis. Laryngoscope. 2018;128(9):2029–33.
41. Liao J, Gan Y, Peng M, Giri M, Yang S, Gu L, et al. GDF15 alleviates the progression of benign tracheobronchial stenosis by inhibiting epithelial-mesenchymal transition and inactivating fibroblasts. Exp Cell Res. 2022;421(2):113410.
42. Duan H, Ma L, Liu H, Zhang Y, Zhang Z, Yan X, et al. Tanshinone IIA attenuates epithelial-mesenchymal transition to inhibit the tracheal narrowing. J Surg Res. 2016;206(1):252–62.
43. Coulis G, Jaime D, Guerrero-Juarez C, Kastenschmidt JM, Farahat PK, Nguyen Q, et al. Single-cell and Spatial transcriptomics identify a macrophage population associated with skeletal muscle fibrosis. Sci Adv. 2023;9(27):eadd9984.
44. Papazoglou A, Huang M, Bulik M, Lafyatis A, Tabib T, Morse C, et al. Epigenetic regulation of profibrotic macrophages in systemic Sclerosis-Associated interstitial lung disease. Arthritis Rheumatol. 2022;74(12):2003–14.
45. Hoeft K, Schaefer GJL, Kim H, Schumacher D, Bleckwehl T, Long Q, et al. Platelet-instructed SPP1(+) macrophages drive myofibroblast activation in fibrosis in a CXCL4-dependent manner. Cell Rep. 2023;42(2):112131.
46. Liu Y, Xun Z, Ma K, Liang S, Li X, Zhou S, et al. Identification of a tumour immune barrier in the HCC microenvironment that determines the efficacy of immunotherapy. J Hepatol. 2023;78(4):770–82.
47. King EM, Zhao Y, Moore CM, Steinhart B, Anderson KC, Vestal B et al. Gpnmb and Spp1 mark a conserved macrophage injury response masking fibrosis-specific programming in the lung. JCI Insight. 2024;9(24).
48. Rodriguez AE, Ducker GS, Billingham LK, Martinez CA, Mainolfi N, Suri V, et al. Serine metabolism supports macrophage IL-1β production. Cell Metab. 2019;29(4):1003–e114.
49. Azwal N, Lokanathan Y, Azman M, Ng MH, Mohamed AS, Baki MM. Serum Interleukin 1β in patients with acquired laryngotracheal stenosis. Acta Otorhinolaryngol Ital. 2022;42(3):250–6.
50. Rauchenwald T, Handle F, Connolly CE, Degen A, Seifarth C, Hermann M, et al. Preadipocytes in human granulation tissue: role in wound healing and response to macrophage polarization. Inflamm Regen. 2023;43(1):53.
51. Amrute JM, Luo X, Penna V, Yang S, Yamawaki T, Hayat S, et al. Targeting immune-fibroblast cell communication in heart failure. Nature. 2024;635(8038):423–33.
52. Ma F, Plazyo O, Billi AC, Tsoi LC, Xing X, Wasikowski R, et al. Single cell and Spatial sequencing define processes by which keratinocytes and fibroblasts amplify inflammatory responses in psoriasis. Nat Commun. 2023;14(1):3455.
53. Theocharidis G, Thomas BE, Sarkar D, Mumme HL, Pilcher WJR, Dwivedi B, et al. Single cell transcriptomic landscape of diabetic foot ulcers. Nat Commun. 2022;13(1):181.
54. Fraser DA, Wang X, Lund J, Nikolić N, Iruarrizaga-Lejarreta M, Skjaeret T, et al. A structurally engineered fatty acid, Icosabutate, suppresses liver inflammation and fibrosis in NASH. J Hepatol. 2022;76(4):800–11.
55. Liu B, Li F, Wang Y, Gao X, Li Y, Wang Y, et al. APP-CD74 axis mediates endothelial cell-macrophage communication to promote kidney injury and fibrosis. Front Pharmacol. 2024;15:1437113.
56. Ye C, Zhu J, Wang J, Chen D, Meng L, Zhan Y, et al. Single-cell and Spatial transcriptomics reveal the fibrosis-related immune landscape of biliary Atresia. Clin Transl Med. 2022;12(11):e1070.

Publisher's note